MNRAS 000, 1–?? (2019) Preprint 7 March 2024 Compiled using MNRAS LATEX style file v3.0

The spatial extension of extended narrow line regions in MaNGA AGN

Jianhang Chen[1,2], Yong Shi[1,2] ⋆, Ross Dempsey[3], David R. Law[4], Yanmei Chen[1,2], Renbin Yan[5], Longji Bing[1,2], Sandro B. Rembold[6,7], Songlin Li[1,2], Xiaoling Yu[1,2], Rogemar A. Riffel[3,6,7], Joe R. Brownstein[8], Rogrio Riffel[7,9]

[1] School of Astronomy and Space Science, Nanjing University, Nanjing 210093, China
[2] Key Laboratory of Modern Astronomy and Astrophysics (Nanjing University), Ministry of Education, Nanjing 210093, China
[3] Department of Physics and Astronomy, Johns Hopkins University, 3400 North Charles Street, Baltimore, MD 21218, USA
[4] Space Telescope Science Institute, 3700 San Martin Drive, Baltimore, MD 21218, USA
[5] Department of Physics and Astronomy, University of Kentucky, 505 Rose Street, Lexington, KY 40506, USA
[6] Departamento de Física, CCNE, Universidade Federal de Santa Maria, 97105-900, Santa Maria, RS, Brazil
[7] Laboratório Interinstitucional de e-Astronomia - LIneA, Rua Gal. José Cristino 77, Rio de Janeiro, RJ - 20921-400, Brazil
[8] Department of Physics and Astronomy, University of Utah, 115 S. 1400 E., Salt Lake City, UT 84112, USA
[9] Departamento de Astronomia, IF, Universidade Federal do Rio Grande do Sul, CP 15051, 91501-970, Porto Alegre, RS, Brazil

arXiv:1908.02885v2 [astro-ph.GA] 23 Sep 2019

Accepted 2019 August 2. Received 2019 July 18

ABSTRACT

In this work, we revisit the size-luminosity relation of the extended narrow line regions (ENLRs) using a large sample of nearby active galactic nuclei (AGN) from the Mapping Nearby Galaxies at Apache Point Observatory (MaNGA) survey. The ENLRs ionized by the AGN are identified through the spatially resolved BPT diagram, which results in a sample of 152 AGN. By combining our AGN with the literature high-luminosity quasars, we found a tight log-linear relation between the size of the ENLR and the AGN [O III]λ5007Å luminosity over four orders of magnitude of the [O III] luminosity. The slope of this relation is 0.42 ± 0.02 which can be explained in terms of a distribution of clouds photoionized by the AGN. This relation also indicates the AGN have the potential to ionize and heat the gas clouds at a large distance from the nuclei without the aids of outflows and jets for the low-luminosity Seyferts. †

Key words: galaxies: ISM, galaxies: nuclei, galaxies: Seyfert, galaxies: statistics

1 INTRODUCTION

It is now generally believed that the super-massive black holes at the centers of galaxies co-evolve with their hosts (Hopkins et al. 2006; Ho 2008; Fabian 2012; Kormendy & Ho 2013; Heckman & Best 2014). An AGN can exert feedbacks on its host galaxy and impact its growth and evolution. This can occur via radiative processes, in which energetic photons from the AGN photoionize and heat gas in the galaxy, or via mechanical processes such as outflows and jets (Osterbrock & Ferland 2006; King & Pounds 2015). Understanding the nature of the feedback is important for improving our knowledge of galaxy formation and evolution.

Based on the unified model of Antonucci (1993), the narrow line region (NLR) is an important and ubiquitous component of AGN. It occurs in a bi-cone away from the obscuring torus, in which the central source illuminates the gas of the host galaxy. In NLRs, the gas density derived from emission line ratios like [S II]λ6716/λ6731Å and [O II]λ3729/λ3726Å is sufficiently low (between 10^2 and 10^3 cm^{-3}) that its emission is dominated by the forbidden-line transitions; the gas temperature calculated from the ratio of [O III]$(\lambda 4959 + \lambda 5007)/\lambda$4363Å is around the photoionization balance temperature of 10^4K; the ionization parameter defined as the ratio between the photon density and the electron density has been mostly set as $U \sim 0.01$ with only 0.5 dex of variation in observations (Bradley et al. 2004; Nesvadba et al. 2008; Osterbrock & Ferland 2006). The size of a NLR is first thought to be sub-kpc scales, but further observations using narrow band images and long-slit spectra revealed some extended ionized nebulae up to several kpc or even tens of kpc in some galaxies (Heckman et al. 1981; McCarthy et al. 1987; Keel et al. 2012; Liu et al. 2013; Obied et al. 2016). These extended nebulae are called the "ex-

⋆ Email: yong@nju.edu.cn
† The code used for this paper is available online https://github.com/cjhang/ENLR

© 2019 The Authors

tended emission line regions" (EELRs) if they are formed by stellar processes, or "extended narrow line regions"(ENLRs) if they are mainly produced by the AGN activity, but the two terms are sometimes mixed in use (Stockton & MacKenty 1987; Unger et al. 1987; Husemann et al. 2013). The ENLR got its name from luminous radio galaxies (Unger et al. 1987) and its formation was thought to be the interaction between the jet and its ambient gas (Heckman et al. 1981; Boroson et al. 1985; Stockton & MacKenty 1987; Fu & Stockton 2009). But further studies have found that many Serfert galaxies also show similar ENLRs (Bennert et al. 2002; Schmitt et al. 2003a,b).

Theoretically, many models have been proposed to explain the formation of (E)NLR. The standard photoionization models assume a set of constant density clouds ionized by a power-law or broken power-law ionizing source (Osterbrock & Ferland 2006), and shock excitation is added for some ENLRs associated with jets (Dopita & Sutherland 1995, 1996; Solórzano-Iñarrea et al. 2001). However, the standard photon-ionization models have several problems. The observed strong coronal lines in some Seyfert galaxies cannot be produced in these models (Dopita et al. 2002; Groves et al. 2004a), and the relationship between the ENLR size and the AGN luminosity has a slope that differs from the predicted value of 0.5 (Schmitt et al. 2003b; Netzer et al. 2004). More recent ENLR models replace the constant density with multicomponent gas densities or include the dust contribution (Dopita et al. 2002; Groves et al. 2004a,b; Dempsey & Zakamska 2018) which produce different slopes of the size-luminosity relation. A better constraint on the slope from the observation is required to distinguish different models.

However, the derived slopes are far from consistent with each other in observations. The observation done by Bennert et al. (2002) found $R_{\rm NLR} \sim L_{[\rm O\,III]}^{0.52\pm0.06}$ that is close to the prediction of the standard photon-ionization model, while Schmitt et al. (2003b) found a much flatter relation with a slope $\sim$ 0.33. Since then, many works have revisited this relation with new observations (Greene et al. 2011; Hainline et al. 2013; Liu et al. 2014; Husemann et al. 2014; Bae et al. 2017; Sun et al. 2018; Fischer et al. 2018), but their derived slopes range from 0.23 to 0.52. The difference may be attributed to their different definitions of the ENLR size, different proxies of the AGN luminosity or different sensitivities. Additionally, most of these works focused on the high-luminosity AGN with a relatively small dynamic range in the AGN luminosity, which limits the accuracy of the derived slope. The advent of integral field unit (IFU) spectroscopy, especially the massive IFU surveys like SDSS-IV/MaNGA (Bundy et al. 2015), offers a new opportunity to measure the size-luminosity relation of ENLRs with a much larger and uniform sample. The spatially resolved spectra also enable us to identify the ENLR by the emission line diagnostics, which is an effective way to isolate the ENLR for low-luminosity AGN. With the large sample available, we can get a better constraint on the slope of size-luminosity relationship of ENLRs in a large dynamic range of AGN luminosity, which can be helpful to answer the formation of ENLRs and to understand the feedback of AGN.

The paper is organized as follows. In section 2, we describe the basic information of MaNGA and sample selection. The methods used to measure the strength of AGN and determine the size of ENLR are described in section 3. The size-luminosity relation of ENLR is described in section 4. Models and possible mechanisms that contribute to the extension of ENLR are discussed in section 5. Finally, we summarize our work in section 6. A flat ΛCDM cosmology with Ω_Λ=0.7, Ω_M=0.3 and $\rm H_0 = 70\,km\,s^{-1}Mpc^{-1}$ is assumed throughout this work.

2 DATA

2.1 MaNGA overview

As one of the three major programs of Sloan Digital Sky Survey IV (SDSS-IV), MaNGA (Bundy et al. 2015; Blanton et al. 2017) uses the 2.5 m Sloan Foundation Telescope (Gunn et al. 2006), aiming at obtaining IFU observations of over 10,000 nearby galaxies from 2014 to 2020 (Law et al. 2015; Drory et al. 2015; Yan et al. 2016a,b). Currently, more than half of the sample has been observed, including 6430 unique targets, some of them have been published as Data Release 15 (DR15) of SDSS-IV (Aguado et al. 2019). All the analyses in this work are based on the eighth internal MaNGA Product Launches (MPL-8).

Each target of MaNGA was observed with one of the specially designed hexagonal bundles ranging from 19 to 127 fibers (Drory et al. 2015), and the spectra were fed to the two BOSS spectrographs with an overall wavelength coverage from 3600 to 10,300Å (Smee et al. 2013). The typical seeing of Apache Point Observatory is 1.5″, but the final spatial resolution of MaNGA is about 2.5″ including the smearing from telescope and instruments, which corresponds to 1-2 kpc at the redshift range of $0.01 < z < 0.15$ (Wake et al. 2017). For the spatial coverage of the bundles, about 30% of the sample has uniform coverage larger than 2.5 effective radii (R_e, the radius containing 50% of the light of the galaxy) and the rest has at least 1.5 R_e. All the data have been reduced by the Data Reduction Pipeline (DRP) (Law et al. 2016) and analyzed by the Data Analysis Pipeline (DAP) (Westfall et al. 2019). Both the software and data are available in the public release (Aguado et al. 2019). All those features make MaNGA the ideal sample for selecting the AGN with extended narrow line regions in nearby universe.

2.2 Sample selection

The most standard way to select the AGN in the optical bands is through the well known BPT diagram (Baldwin et al. 1981; Kauffmann et al. 2003; Ho 2008). It uses the emission line ratios log[O III]λ5007/Hβ vs log[N II]λ6583/Hα or log[S II]$\lambda\lambda$6717, 31/Hα to classify the galaxies as Seyferts, LINERs, star-forming and composite galaxies based on their dominant ionization mechanisms (Baldwin et al. 1981; Kewley et al. 2001; Kauffmann et al. 2003; Kewley et al. 2006). We mainly focused on the [N II]-based BPT diagram, which gives a better separation between the AGN and H II region (Belfiore et al. 2016), but using the [S II]-based BPT diagram does not affect the main results.

Our sample selection method is adapted from Cid Fernandes et al. (2010) and Rembold et al. (2017). We first

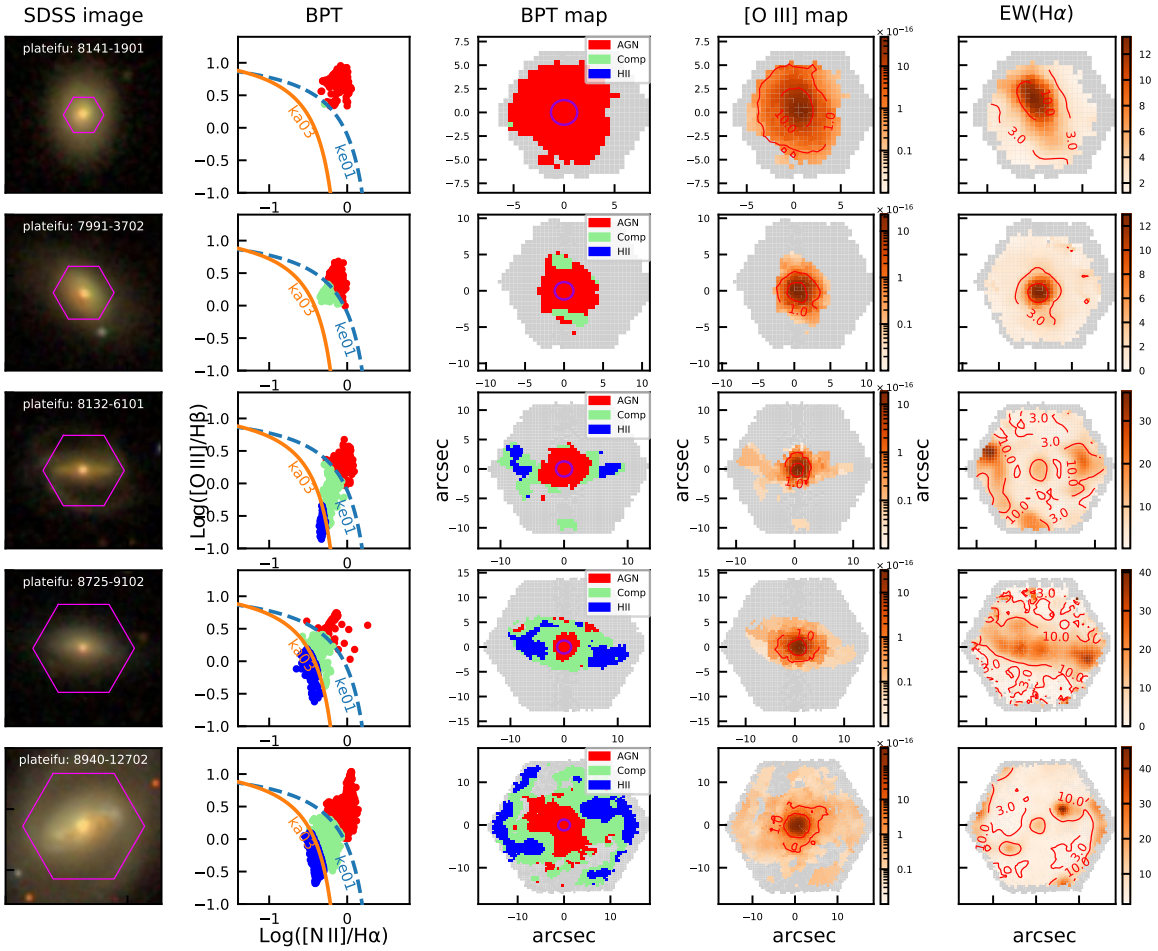


Figure 1. Five example galaxies observed by different bundles of MaNGA. Their fiber numbers are 19, 37, 61, 91, 127 from top to bottom. The bundle edges are indicated by the magenta hexagon in the SDSS RGB images and the grey shaded region in maps. In the second column, we take each spaxel of the galaxy and plot it on the BPT diagram, using the same separation curves as in Fig. 1. These spaxels and their classifications are shown in projection in the third column, We are most interested in spaxels above the Ke01 line, in which the spectra are dominated by AGN activity (Kewley et al. 2001, 2006). The purple circles in the center of each plot in the third column depict the FWHM of the PSF in the g-band. The fourth column are the surface brightness maps of [O III] after attenuation correction, the contours show the value of the surface brightness in units of 10^{-16}erg s^{-1}cm^{-2}arcsec^{-2}. The last column depicts the maps of EW(Hα) in angstrom.

plotted each spaxel within the central radius of 3″ of each MaNGA target on the BPT diagram, and then selected those galaxies with more than 2/3 spaxels classified as AGN. For each galaxy, we only used the spaxels with at least 3 σ detection of all the emission lines needed for the BPT diagram. Additionally, we required the equivalent width (EW) of Hα to be larger than 3Å in order to reduce the contaminations from the diffused ionized gas (DIG) (Cid Fernandes et al. 2010; Lacerda et al. 2018) (also see some discussion in Zhang et al. (2017)). Fig. 1 illustrates five AGN examples along with the BPT maps and EW of Hα maps. Besides DIG, Belfiore et al. (2016) also suggested the central and extended low-ionization regions (LIERs) are more likely to be ionized by diffused stellar sources. Based on their classification, several of our LINER-like AGN belong to the cLIER (central LIER), but since their EW(Hα) are larger than 3Å and unlikely contaminated by stellar radiation, we still included them in our sample. With this method, after removing 16 close merging pairs, we finally found 152 AGN candidates from MPL-8. All the candidates are shown in Fig. 2 and listed in Tab. 1. Both type-I and type-II AGN are selected, but the majority of them are type-II Seyferts. Their average uncorrected [O III]λ5007Å (hereafter [O III]) luminosity is about $10^{40.5}$erg s^{-1}, who mostly belong to low-luminosity Seyferts.

3 METHODS

3.1 Spectrum fitting

The DAP products of MaNGA already provide the full spectrum fitting for each galaxy. The technical details of their "hybrid" approach can be found in Westfall et al. (2019). In brief, three fitting iterations are applied to get the emission lines of each spaxel. For the first iteration, the continuum is binned to reach a global g-band S/N of 10 to get the binned

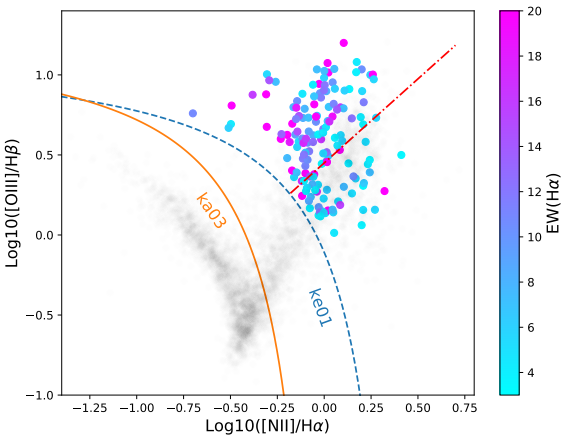


Figure 2. All the AGN candidates selected from MaNGA MPL-8. All the line ratios derived from the median ratio of each galaxy in their central region(within the radius of 3″). Light grey circles (background) show all the MPL-8 galaxies and color coded circles are our selected galaxies with their colors standing for the median EW(Hα) of the central region as before. The solid orange line is the empirical line (Ka03) which separates the star-forming galaxies and the composite (Kauffmann et al. 2003), the blue dashed line (Ke01) is the maximum ionizing boundary of star-forming activity (Kewley et al. 2001) and the red dot-dashed line is the S07 line (Schawinski et al. 2007) which is an empirical separation between Seyferts and LINERs. We did not distinguish between Seyfert and LINER in thiis work, but most of our galaxies are Seyferts according to this line.

stellar kinematics. For the second iteration, the stellar kinematics are kept fixed to model the continuum and emission lines simultaneously in each spaxel. All the emission lines are also modeled with the same kinematics to provide the initial starting guess for the next iteration. Finally, the velocity dispersions of different emission lines are fitted independently but the velocities are constrained to be the same in each spaxel. This fitting results are given in the publicly released products of DR15 (Belfiore et al. 2019).

For the AGN candidates we are interested in, the emission lines generally cannot be modeled well with the single Gaussian profiles used in DR15. We thus fitted the emission lines by adding additional broad components to the Hα and Hβ lines with velocity dispersions larger than 800 km/s to represent the possible signals from broad line regions. To trace possible strong outflow from our AGN, a broad component with velocity dispersions larger than 600 km/s is added to the [O III] doublet during the fitting (Harrison et al. 2014). An example of the full spectrum fitting with broad emission lines is illustrated in Fig. 3. We only accepted the additional broad component when the improvement in the fitting is statistically significant at the 3σ level and pass the F-test.

3.2 The AGN bolometric luminosity

The luminosity of [O III] is often used as a proxy for the AGN bolometric luminosity (Heckman et al. 2004; Kauffmann & Heckman 2009; Heckman & Best 2014). It has been widely used to study the properties of the ENLRs (Husemann et al. 2008, 2014; Sun et al. 2018). To remove star-formation contamination to the AGN [O III] luminosity, we only integrated the emission of AGN-dominated spaxels as identified by the BPT as the total AGN [O III] luminosity. This process is illustrated in the second and third columns of Fig. 1, where the red spaxels of the IFU are dominated by AGN ionization according to Ke01 line (Kewley et al. 2001). The most controversial spaxels are the ones between the Ke01 and the Ka03 lines, which can either be produced by shock excitation or the mixture of AGN and star formation activities. But their contribution to the total [O III] luminosity is small compared to that of the AGN regions, so the [O III] from the composite region is treated as an additional error of the overall [O III] luminosity.

The dust attenuation is corrected by the Balmer decrement and the dust reddening curve of Calzetti (2001), with a assumption of $A_V/E(B-V) = 3.1$ and intrinsic Hα/Hβ ratio of 3.1 (Kewley et al. 2006). The flux maps of Hα and Hβ are rebinned by *VorBin* (Cappellari & Copin 2003) to reach a global S/N of at least 10, and the sigma-clipping of 5 is applied to the derived E(B-V) maps to mask anomalous values. All the remaining analyses are based on the dust corrected [O III] maps.

3.3 The sizes of the extended narrow line regions

The size of ENLRs have been defined in different ways in the literature. Bennert et al. (2002) and Schmitt et al. (2003b) used the Hubble Space Telescope (HST) to obtain narrow band images of [O III], and adopted the maximum 3σ detected radius as the radius of the ENLR. This method is subject to the instrumental sensitivity limit that could be very different in different observations. Studies with long-slit spectroscopic observations define the radius based on isophote (Greene et al. 2011; Hainline et al. 2013, 2014), or the distance at which the ionization state changes from AGN to star-forming activities (Bennert et al. 2006a,b). The long-slit based observations also have drawbacks: the morphology of ENLR is sometimes irregular so that the derived size depends on the orientation of slits (Greene et al. 2011; Husemann et al. 2013). We have compared the measured size based on the IFU and the mock long-slit observation in Fig. 4 following the method discussed below. In most cases, long-slit observations tend to underestimate the true size of ENLR. IFU spectroscopic data allow us to use two-dimensional maps to define the sizes of ENLRs. Common definitions include the radius of a specified [O III] surface brightness isophote (Liu et al. 2013, 2014), or the [O III] flux weighted radius (Husemann et al. 2013, 2014; Bae et al. 2017). We followed the same method as Liu et al. (2013) but chose a different threshold. The isophote threshold of 10^{-15}erg s^{-1}cm^{-2}arcsec^{-2} was used for quasars related studies. This is suitable for such bright objects but are not as useful for fainter Syferts in the our sample as it will leave a large number of AGN undetected. The typical 3 σ depth of the MaNGA observation in [O III] surface brightness can reach 10^{-17}erg s^{-1}cm^{-2}arcsec^{-2}. For our AGN sample, the majority of AGN spaxels have surface brightnesses above 10^{-16}erg s^{-1}cm^{-2}arcsec^{-2} which is thus adopted in this work as the threshold to define the sizes of the ENLRs (hereafter R_{16}). If all spaxels are above this threshold, we extrapolated the fitted [O III] surface brightness profile to determine R_{16} (see Sec. 3.4 for more detail).

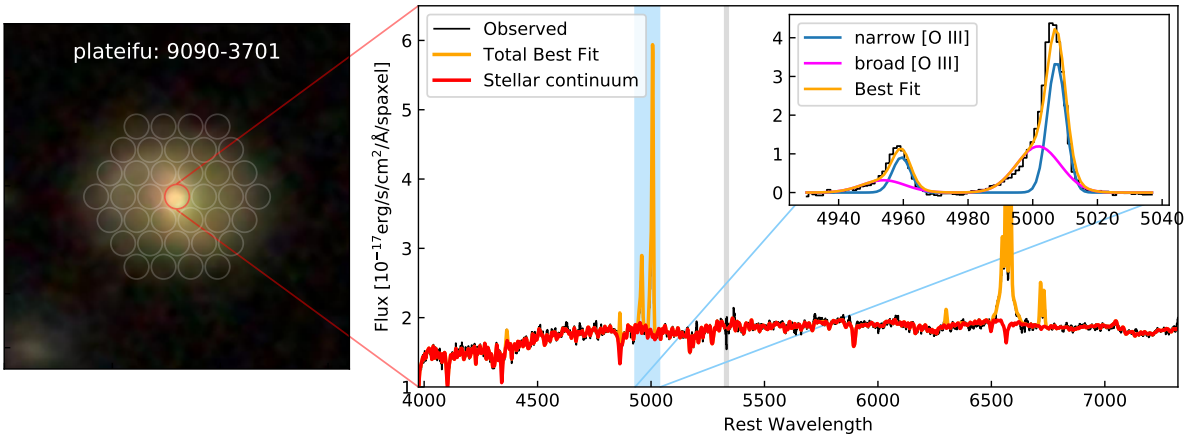


Figure 3. Example of full spectrum fitting with broad emission lines. On the left, it is the SDSS image with fibers superimposed. On the right, it is a spectrum extracted from one of the spaxels belong to the red fiber. The black line shows the observed flux in this spaxel, with the sky lines masked by grey shaded area. The stellar continuum (red) is from DAP hybrid fitting results (Westfall et al. 2019) and the total best fit (orange) is the stellar continuum pluses the fitted emission lines. The zoom-in panel in the right show the emission line fitting results around [O III](the light blue shaded area), with the narrow components in blue and broad components in magenta. The stellar continuum has been subtracted when we fit the emission lines.

It should be noted that the surface brightness can be affected by cosmological dimming, which has a scale factor of $(1+z)^4$ (Liu et al. 2013; Hainline et al. 2014). That is important for works trying to compare sample with different redshift, especially for high redshift quasars.

3.4 Effects of PSF

The spatial properties of MaNGA galaxies are smeared by the seeing from the atmosphere, the telescope and the instruments. The final PSF of each band has been reconstructed by the DRP (Law et al. 2016). To reduce the PSF effects, we first derived the 1-D surface brightness profile of the [O III] maps of AGN spaxels using the Ellipse fitting provided by *Astropy* affiliated package *photutils* (The Astropy Collaboration et al. 2018; Bradley et al. 2017). The profile is then fitted by the Sérsic light distribution:

$$\ln I(r) = \ln I_0 - kr^{1/n}, \quad (1)$$

where the Sérsic index n is kept in the range [0.5, 10] and k in the range [0.01, 10].

Two ways are applied to fit each surface brightness profile. In the first one, the profile is fitted with the Sérsic profle without the PSF, while in the second one, the profile is fitted with the Sérsic profile convolved with a Gaussian modeled g-band PSF, where the FWHM of PSF is provided by the DRP (Law et al. 2016). The fitting results of the first way are taken as the observed profile and the results of second way are regarded as the intrinsic profiles after correcting the PSF. Examples illustrated in Fig. 5 show three surface brightness profiles with different PSF. For the marginally resolved profile (like the first one in Fig 5), its intrinsic profile is severely affected by the PSF and the size differs nearly 50% compared with the observed one. While for those clearly resolved profile (like the last one), its intrinsic and observed profiles remain almost the same with only 6% difference. In most cases, the size derived from the second way is used, but if the fitting iterations of the second way end by reaching the boundaries of parameters, it is labeled as unsuccessful and the radius derived from the first way is used as the upper limit. All the galaxies with failed fitting in the second way are set as unresolved ENLRs in Tab. 1. If both ways failed, 15 galaxies, they are excluded from the later analysis. The uncertainties of all the final radii are the standard deviations calculated by 100 Monte Carlo simulations which randomly adding Gaussian noise to the two dimensional flux map and repeating all the steps mentioned above to re-calculate the radii.

4 THE SIZE-LUMINOSITY RELATION OF ENLR

All the derived data of our sample are summarized in Table 1. Their sizes of ENLRs and luminosities are plotted in Fig. 6 with 1σ error bars. We also included the quasars data from Liu et al. (2013, 2014), which were obtained by the IFU spectroscopic observations on the Gemini telescope and had reached the surface brightness depth of 10^{-16}erg s^{-1}cm^{-2}arcsec^{-2}. It helps to extend our luminosity range from 3 dex to 4 dex, which is important to constrain the slope of the size-luminosity relation. We applied the same method on their derived surface brightness profiles to get R_{16}, but added an additional 20% uncertainty to account for possible errors introduced by the fitting processes. For their [O III] luminosity, 20% error was added for the type-II quasars (Liu et al. 2013) and 10% additional error for type-I quasars (Liu et al. 2014) to account for the errors caused by dust extinction. Law et al. (2018) also provided the R_{16} of their seven IFU observed faint AGN at $z \sim 2$, but it needs the extrapolation to our threshold. The robust error is hard to estimate for their data, so we did not include them in the final fitting. In addition, we also included many other results based on long-slit spectra for comparison. Like the quasars from Greene et al. (2011) and Seyferts from Fraquelli et al. (2003); Bennert et al. (2006a,b). All

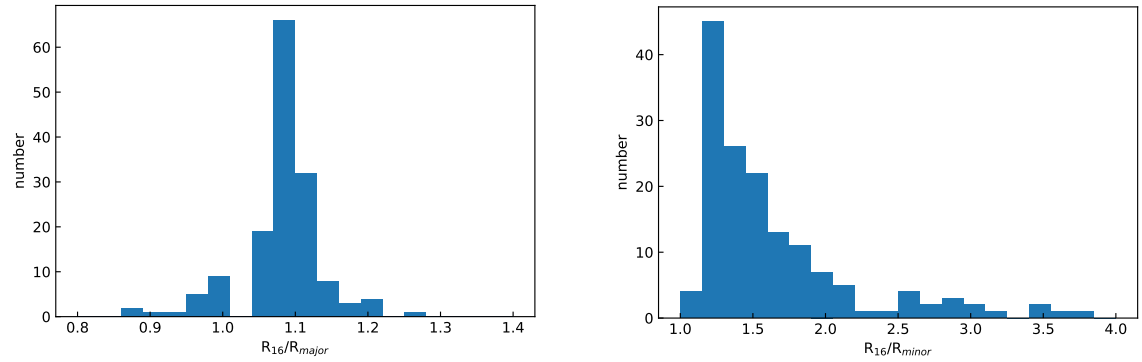


Figure 4. Comparing size measurements based on IFU and mock long-slit observations. Two directions of the long-slit are applied, one aligned with the major axis (left) and the other with the minor axis (right) of the galaxies. The X axis is the ratio between two size at the surface brightness of 10^{-16}erg s^{-1}cm^{-2}arcsec^{-2}.

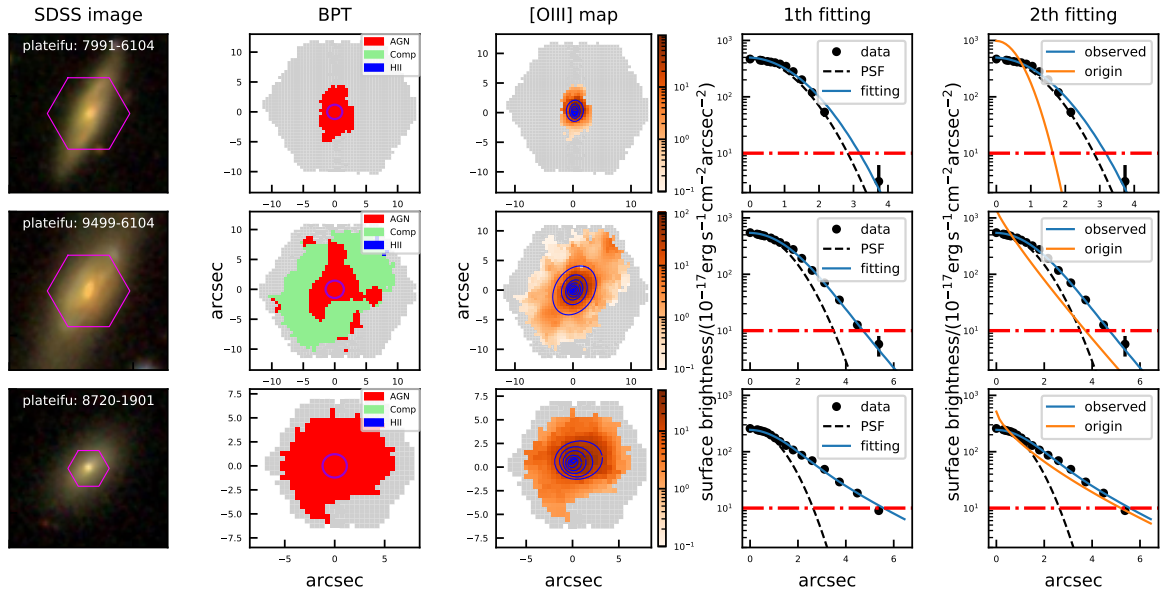


Figure 5. The effects of PSF on the distribution of [O III] surface brightness profile. The first two columns are the same as Fig. 1. The third column also shows the flux map of [O III] as in Fig. 1, but with the fitted isophotes overlaid. The last two columns show the two steps for surface brightness fitting. The black dots are the mean surface brightness of each isophote overlaid on the [O III] map. The blue solid lines are the fitted Sérsic profile, the black dashed line shows the Gaussian modeled PSF of g-band and the orange solid lines show the PSF-corrected surface brightness profile. The red dot-dashed lines are the threshold of surface brightness 10^{-16}erg s^{-1}cm^{-2}arcsec^{-2}. The surface brightness profile of the first target is significantly altered by the PSF, while the third one is almost immune from the PSF. Their size difference between the two fitting at 10^{-16}erg s^{-1}cm^{-2}arcsec^{-2} is 49%, 19% and 6%.

their R_{16} are extrapolated from their power-law fitting results. Based on all the valid IFU observations, a log-linear fit is derived by using the Bayesian method of Kelly (2007). The best-fit solution we have obtained is:

$$\log\left(\frac{R}{\mathrm{pc}}\right) = (0.42\pm0.02)\log\left(\frac{L_{[\mathrm{O\,III}]}}{\mathrm{erg\,s^{-1}}}\right) - (13.97\pm0.95) \quad (2)$$

It is shown in Fig. 6 with 95% confidence interval. The slope derived by our data alone is 0.49 ± 0.04 shown as the dotted line in Fig. 6. This is steeper than some previous studies (Schmitt et al. 2003a; Greene et al. 2011; Liu et al. 2014; Hainline et al. 2014), and more close to 0.5 (Bennert et al. 2002). Since most of the previous results were based on small samples that are limited in the luminosity range, our results should be a better constraint.

Hainline et al. (2014) and Liu et al. (2014) argued that their flattened slope might due to the non-linear relation between the $L_{[\mathrm{O\,III}]}$ and L_{bol}. After replacing the $L_{[\mathrm{O\,III}]}$ with $L_{8\mu\mathrm{m}}$, a slope near 0.44 could be obtained. In order to check the relation between R_{16} with $L_{8\mu\mathrm{m}}$ based on our sample, we cross matched MaNGA with Wide Field Infrared Explorer (WISE) catalog (Wright et al. 2010) and interpolated the $L_{8\mu\mathrm{m}}$ based on photometry at 4.6 μm and 12 μm. As shown in Fig. 7, the overall slope is 0.36 ± 0.03 if including the data from Liu et al. (2013, 2014) and the slope changes to 0.37 ± 0.05 if only our data are used. We caution the reliability of the results based on the IR luminosity, as a significant contribution from star formation is expected to contaminate the $L_{8\mu\mathrm{m}}$ for our Seyferts. Although the SED fitting can be

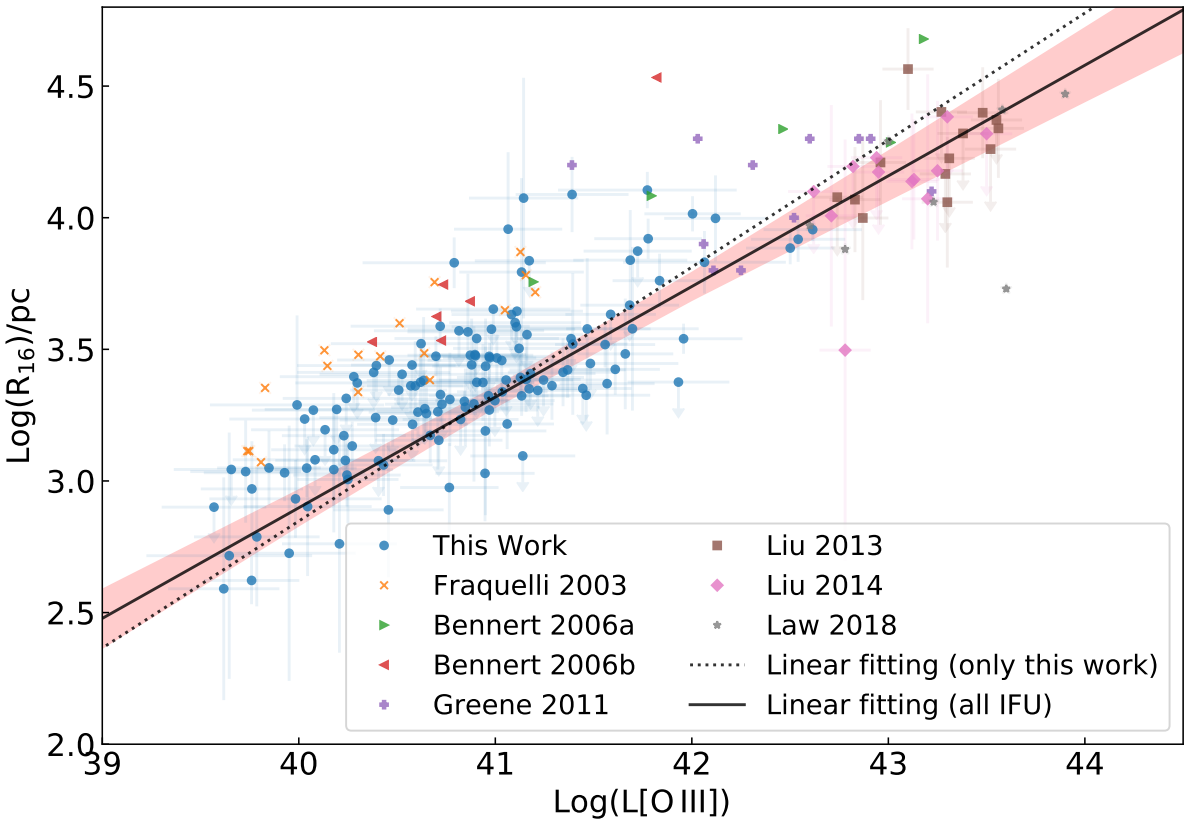


Figure 6. The overall relation between the size of ENLR and luminosity of [O III]. R_{16} is the ENLR size at a surface brightness cut of 10^{-16}erg s^{-1}cm^{-2}arcsec^{-2} and the [O III] luminosity is measured from the AGN region of each galaxy with dust extinction corrected. The data from the AGN candidates in this study are shown in blue circles with 1σ error bars, the undetected galaxies are labeled by upper limits. We also plot the data measured from Seyfert galaxies (Fraquelli et al. 2003; Bennert et al. 2006a,b), luminous quasars (Greene et al. 2011; Liu et al. 2013, 2014) and high redshift faint AGN (Law et al. 2018). But only the IFU data from Liu et al. (2013) and Liu et al. (2014) are included in the fitting. Our best linear fit results in a slope of 0.42 ± 0.02 (black solid line), with the 95% confidence level in light magenta shadow. If only our data is used, the derived slope is 0.49± 0.04 (black dotted line).

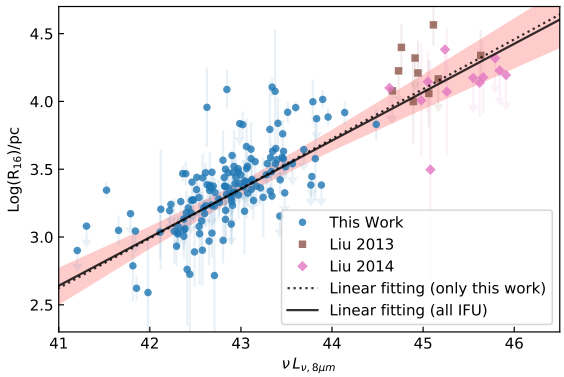


Figure 7. Similar to Fig. 6, but the luminosities have changed to $L_{8\mu m}$. The fitting has a slope of 0.36 ± 0.03 (black solid line) if all the data is used and a slope of 0.37 ± 0.05 (black dotted line) if only our data is used.

used to estimate the star-formation contribution to the IR luminosity, but only a tiny fraction of our sample has far infrared photometry which makes it hard to get a reliable correction.

For the more recent works, Sun et al. (2018) proposed a new method to acquire large samples of AGN with extended [O III] maps. Their [O III] maps were reconstructed from the broad band-images by carefully subtracting the continua, and the extended sizes were defined by the area with a surface brightness larger than 3×10^{-15}erg s^{-1}cm^{-2}arcsec^{-2}. They found a similar slope as Liu et al. (2014) but with a large scatter. Fischer et al. (2018) updated the results of Schmitt et al. (2003b) with 12 new QSOs and obtained a slope of 0.42, which is close to our results. In addition, our results are compatible with Husemann et al. (2014) and Bae et al. (2017) who used the flux weighted size.

At the high luminosity end of the size-luminosity relation, a flattening in slope has been observed (Netzer et al. 2004; Hainline et al. 2013, 2014; Liu et al. 2014), which is usually interpreted as a maximum size of the ENLR. Beyond that radius, the column density may be too low to support [O III] emission (Stern et al. 2016) or photons are mostly obscured by the inner clouds (Dempsey & Zakamska 2018). Since we focused on low luminosity objects with a lower surface brightness cutoff, our results are not sensitive to this upper size limit.

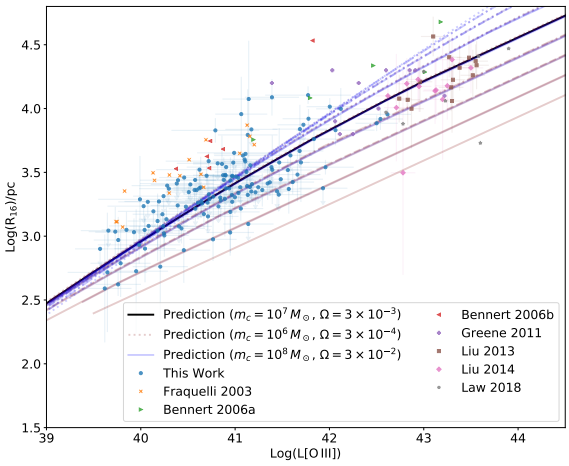


Figure 8. Model predictions of Dempsey & Zakamska (2018) are superimposed on our data points. The black line shows the best fitting model, with cloud mass of $10^7 M_\odot$ and a covering factor of $\Omega = 3 \times 10^{-3}$. Other lines are the models with ± 1 dex variation in the free parameters. Higher cloud mass (m_c) models are shown in blue as clouds mass change from $10^6 M_\odot$ to $10^8 M_\odot$ with colors change from orange to blue. Higher covering factor (Ω) models are shown in thicker lines as covering factor changes from 3×10^{-4} to 3×10^{-2} with lines change from dotted to solid.

5 DISCUSSION

In the standard ionization model, the dimensionless ionization parameter is defined as the ratio between the ionizing photon density and electron density: $U = Q(H_0)/4\pi r^2 c n_e$, where $Q(H_0)$ is the recombination number of hydrogen which is equal to ionizing photons for gas cloud at photoionization equilibrium (Osterbrock & Ferland 2006). Based on the assumption that the ionization parameter and electron density both remain constant along the ENLR, Q is proportional to luminosity, which results in $r \propto L^{0.5}$ (Bennert et al. 2002; Liu et al. 2013; Hainline et al. 2013; Liu et al. 2014). The scenario has been questioned before as some observations appeared to be in conflict with it (Schmitt et al. 2003a; Greene et al. 2011; Liu et al. 2013), but our result over a large dynamic range of the AGN luminosity do not rule out the homogeneous gas model. Recently, Dempsey & Zakamska (2018) proposed a more detailed model of the ENLR. They modeled the (E)NLR as a collection of clouds in pressure equilibrium with the ionizing radiation and the emission line strength like [O III] is calculated by Cloudy (Ferland et al. 1998; Stern et al. 2014). By assuming a cloud distribution $n_c \propto r^{-2}$, they predicted a slope of 0.45 for the size-luminosity of ENLR when using a surface brightness cut of 10^{-15}erg s^{-1}cm^{-2}arcsec^{-2}. If the surface brightness cut at 10^{-16}erg s^{-1}cm^{-2}arcsec^{-2} is adapted, the model fits our data well as shown in Fig. 8. The model takes the masses of clouds (m_c) and their covering factor (Ω) as free parameters. A cloud mass of $10^7 M_\odot$ with a covering factor of 3×10^{-3} fits our data well as the black solid line in Fig. 7. Thus, our data also supports the hypothesis that the ENLR consists of a population of photoionized gas clouds which are sufficiently rarefied to be easily ionized by the central AGN source.

It is widely believed that outflows are prevalent in AGN (Harrison et al. 2014; Woo et al. 2016), and that they can either clear out the ambient gas in the host or compress it at larger distance. Lots of debates have focused on whether or not AGN outflows can suppress star formation of host galaxies (Shi et al. 2009; Zhang et al. 2016; Zubovas & Bourne 2017; Harrison 2017; Harrison et al. 2018; Bing et al. 2018; Gallagher et al. 2019), even for the low luminous AGN (Cheung et al. 2016; Penny et al. 2018). AGN outflows may also affect the extension of the ENLRs by changing the distribution of the gas and dust (Liu et al. 2014; Dempsey & Zakamska 2018). However, there may be a significant difference between the extent of the outflow and the extent of the ENLR. Based on the decomposition of [O III] kinematics, the non-gravitational outflow can be spatially separated in some luminous Seyfert galaxies, and most of them are smaller than the ENLR (Karouzos et al. 2016a,b; Kang & Woo 2018; Fischer et al. 2018). Since the effective radius of an outflow is limited by its energy or momentum, it typically may not reach the size of the ENLR.

Radio-loud AGN can launch powerful jets that survive as conical structures when the jets interact with gas in the ENLR (Baum et al. 1992; Humphrey et al. 2006) and the synchrotron radiation produced by jets make them luminous in the radio band (Sikora et al. 2007; Netzer 2013). An ENLR caused by this effect was the first to be observed since they tend to be highly extended (Boroson et al. 1985; Unger et al. 1987).To pick out the radio-loud galaxies, We match our AGN candidates with the Faint Images of the Radio Sky at Twenty-cm (FIRST) survey (Becker et al. 1995) to get the radio luminosity at 22cm. Following the typical power-law spectral energy distribution with $\alpha = 0.5$, we extrapolated to obtain the $L_v(5\,\mathrm{GHz})$. The radio-loud AGN who most likely possess relatively strong jets are selected by the "radio loudness" $\mathrm{R} = L_v(5\,\mathrm{GHz})/L_v(4400\text{Å}) > 10$ (Netzer 2013). We only found nine radio-loud AGN and seven of them show a compact radio core from the FIRST radio image. Even though 5/9 galaxies show asymmetrical ENLRs, all of them follow the overall log-linear relation between the luminosity and size of ENLRs. Both the number of radio-loud AGN in our sample and their ENLR sizes These results suggest that the jets may not be the main trigger of ENLR thus have limited influence on the global size-luminosity relation of ENLR.

6 CONCLUSIONS

In this work, an IFU-based emission line diagnostics is used to identify the ENLRs and a sample of 152 AGN candidates have been found in MaNGA internal data release of MPL-8 with the ENLR features. Most of the candidates are low-luminosity Seyferts but span about three orders of magnitude in the AGN [O III] luminosity. The key points of this work are listed as follows:

(i) Based on a surface brightness cut of 10^{-16}erg s^{-1}cm^{-2}arcsec^{-2}, we confirmed the log-linear relation between size and luminosity of ENLR over four orders of magnitude of the AGN [O III] luminosity including high luminous quasars . The slope derived by the IFU data is 0.42 ± 0.02, which is more consistent with the model that the ENLR is filled by a population of photoionized clouds (Dempsey & Zakamska 2018).

(ii) Kinematic feedbacks have limited influence on the global size-luminosity relation of ENLR in the low luminosity range, as the regions detected outflow mostly smaller than the ENLRs and the radio-loud AGN do not show a more extended ENLRs.

ACKNOWLEDGEMENTS

The authors thank Xiaotong Guo for great help for the SED fitting. This work is supported by the National Key R&D Program of China (No. 2018YFA0404502, No. 2017YFA0402704), the National Natural Science Foundation of China (NSFC grants 11825302, 11733002 and 11773013) and the Excellent Youth Foundation of the Jiangsu Scientific Committee (BK20150014).

SBR and RAR acknowledge partial financial support by Fundação de Amparo à pesquisa do Estado do RS (FAPERGS). RR thanks CNPq, FAPERGS and CAPES for partial financial supporting this project.

Funding for the Sloan Digital Sky Survey IV has been provided by the Alfred P. Sloan Foundation, the U.S. Department of Energy Office of Science, and the Participating Institutions. SDSS acknowledges support and resources from the Center for High-Performance Computing at the University of Utah. The SDSS web site is www.sdss.org. SDSS is managed by the Astrophysical Research Consortium for the Participating Institutions of the SDSS Collaboration including the Brazilian Participation Group, the Carnegie Institution for Science, Carnegie Mellon University, the Chilean Participation Group, the French Participation Group, Harvard-Smithsonian Center for Astrophysics, Instituto de Astrofsica de Canarias, The Johns Hopkins University, Kavli Institute for the Physics and Mathematics of the Universe (IPMU) / University of Tokyo, the Korean Participation Group, Lawrence Berkeley National Laboratory, Leibniz Institut fr Astrophysik Potsdam (AIP), Max-Planck-Institut fr Astronomie (MPIA Heidelberg), Max-Planck-Institut fr Astrophysik (MPA Garching), Max-Planck-Institut fr Extraterrestrische Physik (MPE), National Astronomical Observatories of China, New Mexico State University, New York University, University of Notre Dame, Observatrio Nacional / MCTI, The Ohio State University, Pennsylvania State University, Shanghai Astronomical Observatory, United Kingdom Participation Group, Universidad Nacional Autnoma de Mxico, University of Arizona, University of Colorado Boulder, University of Oxford, University of Portsmouth, University of Utah, University of Virginia, University of Washington, University of Wisconsin, Vanderbilt University, and Yale University.

This research made use of: `NumPy`, a fundamental package for scientific computing with Python (van der Walt et al. 2011); `SciPy`, an open source scientific tool for Python (Jones et al. 01); `Matplotlib`, a 2-D plotting library for Python (Hunter 2007); `Astropy`, a community-developed core Python package for astronomy (The Astropy Collaboration et al. 2018); `IPython`, an interactive computing system for Python (Perez & Granger 2007); `photutils`, an affiliated package of `AstroPy` to provide tools for detecting and performing photometry of astronomical sources (Bradley et al. 2017); `pPXF` a software using a maximum penalized likelihood approach to extract the stellar kinematics or stellar population from absorption-line spectra of galaxies (Cappellari & Emsellem 2004; Cappellari 2017); `VorBin` a package adaptively spatial bin two-dimensional data to a constant signal-to-noise ratio per bin (Cappellari & Copin 2003); `Marvin` a toolkit for streamlined access and visualization of the SDSS-IV MaNGA data set (Cherinka et al. 2018).

REFERENCES

Aguado D. S., et al., 2019, ApJS, 240, 23
Antonucci R., 1993, ARA&A, 31, 473
Bae H.-J., Woo J.-H., Karouzos M., Gallo E., Flohic H., Shen Y., Yoon S.-J., 2017, ApJ, 837, 91
Baldwin J. A., Phillips M. M., Terlevich R., 1981, PASP, 93, 5
Baum S. A., Heckman T. M., van Breugel W., 1992, ApJ, 389, 208
Becker R. H., White R. L., Helfand D. J., 1995, ApJ, 450, 559
Belfiore F., et al., 2016, MNRAS, 461, 3111
Belfiore F., et al., 2019, arXiv e-prints,
Bennert N., Falcke H., Schulz H., Wilson A. S., Wills B. J., 2002, ApJ, 574, L105
Bennert N., Jungwiert B., Komossa S., Haas M., Chini R., 2006a, A&A, 456, 953
Bennert N., Jungwiert B., Komossa S., Haas M., Chini R., 2006b, A&A, 459, 55
Bing L., et al., 2018, MNRAS,
Blanton M. R., et al., 2017, AJ, 154, 28
Boroson T. A., Persson S. E., Oke J. B., 1985, ApJ, 293, 120
Bradley L. D., Kaiser M. E., Baan W. A., 2004, ApJ, 603, 463
Bradley L., et al., 2017, astropy/photutils: v0.4, doi:10.5281/zenodo.1039309, `https://doi.org/10.5281/zenodo.1039309`
Bundy K., et al., 2015, ApJ, 798, 7
Calzetti D., 2001, PASP, 113, 1449
Cappellari M., 2017, MNRAS, 466, 798
Cappellari M., Copin Y., 2003, MNRAS, 342, 345
Cappellari M., Emsellem E., 2004, PASP, 116, 138
Cherinka B., et al., 2018, arXiv e-prints,
Cheung E., et al., 2016, Nature, 533, 504
Cid Fernandes R., Stasińska G., Schlickmann M. S., Mateus A., Vale Asari N., Schoenell W., Sodré L., 2010, MNRAS, 403, 1036
Dempsey R., Zakamska N. L., 2018, MNRAS, 477, 4615
Dopita M. A., Sutherland R. S., 1995, ApJ, 455, 468
Dopita M. A., Sutherland R. S., 1996, ApJS, 102, 161
Dopita M. A., Groves B. A., Sutherland R. S., Binette L., Cecil G., 2002, ApJ, 572, 753
Drory N., et al., 2015, AJ, 149, 77
Fabian A. C., 2012, ARA&A, 50, 455
Ferland G. J., Korista K. T., Verner D. A., Ferguson J. W., Kingdon J. B., Verner E. M., 1998, PASP, 110, 761
Fischer T. C., et al., 2018, ApJ, 856, 102
Fraquelli H. A., Storchi-Bergmann T., Levenson N. A., 2003, MNRAS, 341, 449
Fu H., Stockton A., 2009, ApJ, 690, 953
Gallagher R., Maiolino R., Belfiore F., Drory N., Riffel R., Riffel R. A., 2019, MNRAS, 485, 3409
Greene J. E., Zakamska N. L., Ho L. C., Barth A. J., 2011, ApJ, 732, 9
Groves B. A., Dopita M. A., Sutherland R. S., 2004a, ApJS, 153, 9
Groves B. A., Dopita M. A., Sutherland R. S., 2004b, ApJS, 153, 75
Gunn J. E., et al., 2006, AJ, 131, 2332
Hainline K. N., Hickox R., Greene J. E., Myers A. D., Zakamska N. L., 2013, ApJ, 774, 145

Hainline K. N., Hickox R. C., Greene J. E., Myers A. D., Zakamska N. L., Liu G., Liu X., 2014, ApJ, 787, 65
Harrison C. M., 2017, Nature Astronomy, 1, 0165
Harrison C. M., Alexander D. M., Mullaney J. R., Swinbank A. M., 2014, MNRAS, 441, 3306
Harrison C. M., Costa T., Tadhunter C. N., Flütsch A., Kakkad D., Perna M., Vietri G., 2018, Nature Astronomy, 2, 198
Heckman T. M., Best P. N., 2014, ARA&A, 52, 589
Heckman T. M., Miley G. K., van Breugel W. J. M., Butcher H. R., 1981, ApJ, 247, 403
Heckman T. M., Kauffmann G., Brinchmann J., Charlot S., Tremonti C., White S. D. M., 2004, ApJ, 613, 109
Ho L. C., 2008, ARA&A, 46, 475
Hopkins P. F., Hernquist L., Cox T. J., Di Matteo T., Robertson B., Springel V., 2006, ApJS, 163, 1
Humphrey A., Villar-Martín M., Fosbury R., Vernet J., di Serego Alighieri S., 2006, MNRAS, 369, 1103
Hunter J. D., 2007, Computing in Science Engineering, 9, 90
Husemann B., Wisotzki L., Sánchez S. F., Jahnke K., 2008, A&A, 488, 145
Husemann B., Wisotzki L., Sánchez S. F., Jahnke K., 2013, A&A, 549, A43
Husemann B., Jahnke K., Sánchez S. F., Wisotzki L., Nugroho D., Kupko D., Schramm M., 2014, MNRAS, 443, 755
Jones E., Oliphant T., Peterson P., et al., 2001–, SciPy: Open source scientific tools for Python, http://www.scipy.org/
Kang D., Woo J.-H., 2018, The Astrophysical Journal, 864, 124
Karouzos M., Woo J.-H., Bae H.-J., 2016a, ApJ, 819, 148
Karouzos M., Woo J.-H., Bae H.-J., 2016b, ApJ, 833, 171
Kauffmann G., Heckman T. M., 2009, MNRAS, 397, 135
Kauffmann G., et al., 2003, MNRAS, 346, 1055
Keel W. C., et al., 2012, MNRAS, 420, 878
Kelly B. C., 2007, ApJ, 665, 1489
Kewley L. J., Dopita M. A., Sutherland R. S., Heisler C. A., Trevena J., 2001, ApJ, 556, 121
Kewley L. J., Groves B., Kauffmann G., Heckman T., 2006, MNRAS, 372, 961
King A., Pounds K., 2015, ARA&A, 53, 115
Kormendy J., Ho L. C., 2013, ARA&A, 51, 511
Lacerda E. A. D., et al., 2018, MNRAS, 474, 3727
Law D. R., et al., 2015, AJ, 150, 19
Law D. R., et al., 2016, AJ, 152, 83
Law D. R., Steidel C. C., Chen Y., Strom A. L., Rudie G. C., Trainor R. F., 2018, ApJ, 866, 119
Liu G., Zakamska N. L., Greene J. E., Nesvadba N. P. H., Liu X., 2013, MNRAS, 430, 2327
Liu G., Zakamska N. L., Greene J. E., 2014, MNRAS, 442, 1303
McCarthy P. J., van Breugel W., Spinrad H., Djorgovski S., 1987, ApJ, 321, L29
Nesvadba N. P. H., Lehnert M. D., De Breuck C., Gilbert A. M., van Breugel W., 2008, A&A, 491, 407
Netzer H., 2013, The Physics and Evolution of Active Galactic Nuclei
Netzer H., Shemmer O., Maiolino R., Oliva E., Croom S., Corbett E., di Fabrizio L., 2004, ApJ, 614, 558
Obied G., Zakamska N. L., Wylezalek D., Liu G., 2016, MNRAS, 456, 2861
Osterbrock D. E., Ferland G. J., 2006, Astrophysics of gaseous nebulae and active galactic nuclei. University Science Books
Penny S. J., et al., 2018, MNRAS, 476, 979
Perez F., Granger B. E., 2007, Computing in Science Engineering, 9, 21
Rembold S. B., et al., 2017, MNRAS, 472, 4382
Schawinski K., Thomas D., Sarzi M., Maraston C., Kaviraj S., Joo S.-J., Yi S. K., Silk J., 2007, MNRAS, 382, 1415
Schmitt H. R., Donley J. L., Antonucci R. R. J., Hutchings J. B., Kinney A. L., 2003a, ApJS, 148, 327
Schmitt H. R., Donley J. L., Antonucci R. R. J., Hutchings J. B., Kinney A. L., Pringle J. E., 2003b, ApJ, 597, 768
Shi Y., Rieke G. H., Ogle P., Jiang L., Diamond-Stanic A. M., 2009, ApJ, 703, 1107
Sikora M., Stawarz Ł., Lasota J.-P., 2007, ApJ, 658, 815
Smee S. A., et al., 2013, AJ, 146, 32
Solórzano-Iñarrea C., Tadhunter C. N., Axon D. J., 2001, MNRAS, 323, 965
Stern J., Laor A., Baskin A., 2014, MNRAS, 438, 901
Stern J., Faucher-Giguère C.-A., Zakamska N. L., Hennawi J. F., 2016, ApJ, 819, 130
Stockton A., MacKenty J. W., 1987, ApJ, 316, 584
Sun A.-L., et al., 2018, MNRAS,
The Astropy Collaboration et al., 2018, preprint, (arXiv:1801.02634)
Unger S. W., Pedlar A., Axon D. J., Whittle M., Meurs E. J. A., Ward M. J., 1987, MNRAS, 228, 671
Wake D. A., et al., 2017, AJ, 154, 86
Westfall K. B., et al., 2019, arXiv e-prints,
Woo J.-H., Bae H.-J., Son D., Karouzos M., 2016, ApJ, 817, 108
Wright E. L., et al., 2010, AJ, 140, 1868
Yan R., et al., 2016a, AJ, 151, 8
Yan R., et al., 2016b, AJ, 152, 197
Zhang Z., Shi Y., Rieke G. H., Xia X., Wang Y., Sun B., Wan L., 2016, ApJ, 819, L27
Zhang K., et al., 2017, MNRAS, 466, 3217
Zubovas K., Bourne M. A., 2017, MNRAS, 468, 4956
van der Walt S., Colbert S. C., Varoquaux G., 2011, Computing in Science Engineering, 13, 22

Table 1. All the AGN candidates with extended narrow line region

plateifu	ra degree	dec degree	z	g_{PSF}(FWHM) arcsec	$\log L_{[O\,III]}$ erg/s	$\log L_{8\mu m}$ erg/s	$\log L_{1.4GHz}$ erg/s	R_{15} (kpc)	R_{16} (kpc)	resolved	radio loudness
7495-1902	205.044769	26.841041	0.0318073	2.32	39.66±0.29	41.84	nan	nan	3.04±0.06	False	0.00
7815-6104	319.193099	11.043741	0.0806967	2.41	42.62±0.25	43.60	38.64	6.51±0.85	9.01±0.90	True	1.81
7991-6104	258.827410	57.658770	0.0282021	2.40	40.61±0.25	42.34	nan	nan	3.26±0.23	False	0.00
7991-3702	258.158752	57.322421	0.0266298	2.40	40.43±0.25	42.39	nan	0.43±0.32	1.15±0.31	True	0.00
8132-6101	111.733682	41.026691	0.129403	2.57	41.72±0.28	43.83	nan	nan	3.87±0.20	False	0.00
8247-6101	136.089598	41.481729	0.0244671	2.72	39.93±0.41	42.31	37.34	nan	1.07±0.27	True	0.33
8137-3702	115.368720	44.408794	0.131997	3.01	42.00±0.25	43.90	nan	1.38±1.45	10.35±1.59	True	0.00
8141-1901	117.472421	45.248483	0.0312591	2.61	40.97±0.24	42.36	nan	0.93±0.36	2.94±0.38	True	0.00
8143-6101	121.014201	40.802613	0.126168	2.52	42.12±0.26	43.79	39.75	5.34±1.35	9.94±3.74	True	8.27
8256-12704	166.129408	42.624554	0.12611	2.43	41.84±0.24	43.46	38.98	2.27±1.41	5.77±1.36	True	1.22
8249-3704	137.874763	45.468320	0.0268253	2.52	40.88±0.32	42.94	37.88	0.86±0.36	2.76±1.12	True	2.26
8319-12705	202.128436	47.714038	0.0607597	2.54	40.62±0.46	43.07	nan	nan	3.52±0.48	False	0.00
8341-12704	189.213253	45.651170	0.030345	2.56	40.88±0.52	42.83	38.00	0.06±0.19	1.35±0.57	True	0.49
8439-6104	143.510355	50.027486	0.0378229	2.47	40.77±0.28	42.97	38.53	0.58±0.82	2.04±0.83	True	1.92
8452-1901	155.885556	46.057755	0.0257723	2.52	40.04±0.25	41.66	nan	nan	1.12±0.28	True	0.00
8483-12703	245.248314	49.001777	0.0582143	2.42	40.20±46.90	42.40	nan	nan	1.51±0.60	True	0.00
8482-12704	243.581821	50.465611	0.0602584	2.44	40.82±10.38	42.93	39.99	0.48±0.62	2.14±0.62	True	24.95
8549-12701	240.470871	45.351940	0.0420468	2.36	41.13±0.32	42.94	38.31	1.02±0.47	2.47±0.47	True	1.13
8465-12704	198.141843	48.366614	0.0558079	2.42	41.07±0.28	42.63	38.32	0.44±0.63	9.05±6.09	True	2.06
8552-12701	226.431661	44.404902	0.0283402	2.59	40.48±0.55	43.06	nan	0.27±0.46	3.20±2.70	True	0.00
8552-9102	229.308914	44.018031	0.12226	2.57	40.46±0.27	43.28	nan	nan	3.46±0.41	False	0.00
8318-3704	197.891834	44.933078	0.0247632	2.38	40.25±0.27	42.31	37.78	0.37±0.29	1.05±0.29	True	1.41
8318-6102	197.239319	45.905447	0.12908	2.35	41.78±0.27	43.51	39.87	2.43±1.51	8.32±1.46	True	11.83
8464-6101	186.180997	44.410771	0.125582	2.48	42.54±0.24	44.14	39.62	5.23±1.38	8.28±1.64	True	8.35
8320-3704	206.612456	22.076742	0.0275673	2.38	40.23±0.32	41.79	nan	nan	3.17±0.18	False	0.00
8550-3704	248.426386	39.185120	0.0298414	2.50	40.39±0.29	42.23	37.48	nan	3.24±0.21	False	0.43
8606-12701	255.029870	37.839502	0.0633343	2.58	40.95±0.31	43.04	nan	nan	1.55±1.14	True	0.00
8314-3704	243.155037	39.419024	0.0321959	2.37	39.85±0.26	42.37	nan	nan	1.12±0.36	True	0.00
8611-3704	262.996722	59.971638	0.0291196	2.54	40.13±0.38	42.22	37.42	nan	3.19±0.17	False	0.67
7992-9102	254.542084	62.415648	0.119399	2.54	41.69±0.29	43.41	38.78	2.58±2.02	6.90±3.02	True	1.30
8603-6101	247.159333	39.551266	0.0311758	2.62	39.76±0.26	42.65	39.80	nan	0.93±0.39	True	20.48
8612-12704	254.564575	39.391464	0.0343116	2.52	41.68±0.25	43.06	38.13	nan	3.67±0.37	False	1.10
8588-12704	249.557306	40.146821	0.030363	2.51	40.71±0.31	42.90	37.53	0.41±0.52	1.83±0.93	True	0.28
8602-12701	247.048171	39.821898	0.0267882	2.54	40.27±0.29	42.37	37.24	0.27±0.30	1.36±0.29	True	0.13
8077-6103	39.446587	0.405085	0.0473019	2.59	40.53±0.42	42.46	nan	nan	3.41±0.31	False	0.00
8147-6102	118.627843	25.815986	0.0631476	2.67	40.38±0.39	43.11	nan	nan	3.41±0.00	False	0.00
8146-12705	118.053214	28.772580	0.0636542	2.46	40.18±0.32	42.57	nan	nan	1.31±0.65	True	0.00
8084-6103	50.741676	0.054137	0.035737	2.53	40.03±0.38	42.68	37.68	nan	3.24±0.25	False	0.96
8718-12702	120.700706	45.034554	0.038928	2.49	41.03±0.38	43.00	38.17	nan	3.46±0.44	False	0.83
8718-12701	119.182152	44.856709	0.04992	2.45	40.87±0.32	42.68	nan	nan	3.48±0.40	False	0.00

Table 1 – *continued*

plateifu	ra degree	dec degree	z	g_{PSF}(FWHM) arcsec	$\log L_{[O\,III]}$ erg/s	$\log L_{8\mu m}$ erg/s	$\log L_{1.4GHz}$ erg/s	R_{15} (kpc)	R_{16} (kpc)	resolved	radio loudness
8725-9102	127.178094	45.742555	0.049053	2.63	41.12±0.34	42.97	nan	nan	3.50±0.30	False	0.00
10001-6102	132.653992	57.359668	0.0261046	2.59	40.86±0.31	42.80	37.56	0.38±0.38	3.68±1.87	True	0.47
8715-3702	119.920672	50.839973	0.0543641	2.60	42.50±0.22	43.96	39.66	3.46±0.71	7.67±1.09	True	33.51
8255-6101	166.509879	43.173473	0.0584258	2.66	40.85±0.38	42.76	38.50	0.69±0.77	1.91±0.64	True	1.94
8241-9102	127.170800	17.581400	0.0665263	2.44	41.13±0.32	43.32	38.80	0.49±1.68	6.22±5.11	True	3.62
8241-6102	126.059633	17.331951	0.0372518	2.52	41.48±0.45	43.78	38.65	nan	3.45±0.32	False	2.10
8720-1901	121.147928	50.708556	0.0227214	2.43	40.51±0.25	41.52	nan	0.62±0.26	2.21±0.29	True	0.00
8547-12701	217.629971	52.707159	0.0448811	2.55	41.37±0.30	43.43	38.46	1.61±0.49	2.64±0.65	True	1.17
8978-12705	249.558611	41.938810	0.0286035	2.42	39.98±0.71	42.83	nan	nan	1.57±0.75	True	0.00
8978-6102	249.371986	40.879947	0.0263847	2.44	38.72±16.91	42.61	37.44	nan	nan	True	0.65
8978-9101	247.907996	41.493643	0.0303346	2.51	39.98±0.51	42.45	nan	nan	3.18±0.22	False	0.00
8979-6102	241.823389	41.403604	0.0346392	2.28	40.04±0.33	42.58	nan	nan	0.80±0.49	True	0.00
8948-12704	167.306020	49.519432	0.0724271	2.42	41.11±0.33	43.32	38.60	nan	3.59±0.28	False	1.41
8946-3701	168.957727	46.319564	0.0532814	2.40	40.90±0.26	42.97	nan	nan	3.48±0.25	False	0.00
8947-3701	168.947800	50.401634	0.0473068	2.34	40.97±0.25	43.14	nan	0.83±0.54	1.86±0.59	True	0.00
8945-3703	173.911234	47.515520	0.045503	2.66	40.26±1.44	42.55	nan	nan	1.06±0.91	True	0.00
8597-3703	224.749647	48.409855	0.0358627	2.48	40.30±0.32	42.66	38.25	nan	3.37±0.44	False	0.90
9026-9101	249.318419	44.418230	0.0314197	2.56	40.91±0.29	42.82	37.88	nan	3.37±0.35	False	0.36
9049-1901	247.560973	26.206474	0.131457	2.47	42.06±0.41	44.49	39.65	4.36±1.36	6.77±1.85	True	8.35
9002-12702	222.810069	30.692246	0.0547198	2.47	40.25±nan	42.83	nan	nan	3.50±0.63	False	0.00
9031-1902	241.029075	44.549765	0.0429606	2.68	40.72±0.27	42.71	nan	0.54±0.50	2.13±0.52	True	0.00
9027-12704	245.346647	32.349014	0.034659	2.38	41.13±0.25	42.90	37.93	0.90±0.37	2.11±0.37	True	0.72
8982-3703	203.190094	26.580376	0.0470053	2.43	41.57±0.24	43.03	39.17	1.21±0.58	2.34±1.04	True	49.44
7972-6103	315.831306	10.944169	0.0431534	2.55	40.59±1.17	42.71	39.54	0.15±0.43	1.69±0.50	True	20.07
9025-12704	246.050764	30.162261	0.0482447	2.46	40.62±0.31	42.70	nan	0.28±0.53	2.37±0.59	True	0.00
7958-9101	258.495841	33.607137	0.0386619	2.44	40.64±0.29	42.66	38.11	0.58±0.51	2.41±1.33	True	4.74
9195-3703	29.052229	14.906639	0.026913	2.58	41.18±0.33	43.04	nan	nan	3.41±0.43	False	0.00
8080-12703	49.487801	-0.169101	0.0227967	2.60	39.99±0.44	42.90	38.44	nan	1.94±1.52	True	1.42
9182-6102	119.486337	39.993365	0.0657771	2.36	41.59±0.23	43.35	40.15	nan	3.63±0.44	False	66.91
9193-12701	45.954624	-1.103750	0.0136253	2.47	40.84±0.23	43.34	36.93	0.83±0.15	2.01±0.18	True	0.16
8940-12702	120.087418	26.613527	0.0267379	2.56	41.56±0.25	43.49	37.84	0.60±0.40	3.30±0.66	True	0.30
9183-3703	121.920806	39.004239	0.0233453	2.73	41.04±0.23	43.32	38.20	0.43±0.26	2.18±0.27	True	1.66
8993-12705	165.391531	45.653868	0.0294089	2.53	41.96±0.30	43.38	38.40	1.71±0.32	3.47±0.46	True	1.02
8992-3702	171.657262	51.573041	0.0264158	2.68	40.21±0.29	42.41	nan	nan	0.58±0.55	True	0.00
9485-12705	121.779937	36.233479	0.0323135	2.48	41.25±0.33	43.88	nan	nan	3.38±1.38	False	0.00
9487-3702	123.330544	46.147157	0.053819	2.42	40.90±0.24	42.92	nan	nan	3.48±0.30	False	0.00
8989-3703	177.440360	50.527016	0.026442	2.45	40.77±0.25	42.80	nan	0.19±0.32	0.94±0.37	True	0.00
8984-9102	203.850240	27.911890	0.0268301	2.38	39.98±0.44	42.29	nan	nan	0.86±0.29	True	0.00
8983-12701	203.830208	26.424781	0.0253738	2.58	40.46±0.28	42.49	nan	0.35±0.47	0.78±0.46	True	0.00
8311-6104	205.282731	23.282055	0.0263526	2.70	41.46±0.33	43.48	38.87	nan	3.33±0.10	False	5.39

Table 1 – *continued*

plateifu	ra degree	dec degree	z	g_{PSF}(FWHM) arcsec	$\log L_{[O\,III]}$ erg/s	$\log L_{8\mu m}$ erg/s	$\log L_{1.4GHz}$ erg/s	R_{15} (kpc)	R_{16} (kpc)	resolved	radio loudness
8309-12701	208.289083	51.812501	0.067572	2.46	40.91±0.42	43.29	38.49	nan	3.54±0.33	False	1.56
9507-12704	129.600037	25.754501	0.0181814	2.50	40.71±0.32	43.43	38.99	nan	3.15±0.20	False	8.42
9507-12705	129.520694	25.329505	0.0281762	2.50	40.67±0.27	42.60	nan	0.82±0.33	1.49±0.36	True	0.00
9508-12704	127.105954	26.397370	0.0808831	2.29	40.98±0.43	43.47	38.73	nan	3.58±0.24	False	1.52
9508-3704	127.107818	25.014635	0.0287366	2.38	40.73±0.29	42.54	nan	nan	3.29±0.27	False	0.00
9024-12705	223.867459	32.840028	0.0601609	2.39	40.89±0.40	43.24	38.68	0.18±0.48	1.96±1.33	True	1.03
9488-3702	126.216411	20.991216	0.0228872	2.36	39.62±0.28	41.98	nan	nan	0.39±0.38	True	0.00
9502-9101	128.341931	25.104925	0.0866	2.41	40.40±140.78	43.11	39.11	nan	3.65±1.02	False	2.91
9502-12703	129.545574	24.895295	0.0286559	2.46	41.93±0.26	43.17	39.22	nan	3.38±0.25	False	7.59
9511-12704	129.312117	4.695876	0.0469711	2.44	40.97±0.32	42.86	nan	nan	3.47±0.40	False	0.00
9511-6104	129.362363	3.955690	0.0470113	2.46	40.07±0.31	42.45	37.79	nan	3.27±0.25	False	1.11
8990-12705	173.537567	49.254562	0.037232	2.33	41.01±0.25	42.39	nan	0.75±0.43	2.93±0.60	True	0.00
8990-9101	173.933151	49.037649	0.0296172	2.37	39.65±0.42	42.71	38.03	nan	0.52±0.56	True	2.18
8442-9102	200.222837	32.190761	0.0230284	2.49	40.58±0.28	42.42	nan	nan	3.22±0.23	False	0.00
9048-1902	246.255977	24.263156	0.0503021	2.55	41.61±0.23	43.12	37.99	0.40±0.63	2.65±0.59	True	1.02
9095-12701	241.913639	23.416866	0.0874596	2.36	40.82±0.43	43.40	nan	nan	3.57±0.02	False	0.00
9196-12703	262.399283	54.494424	0.0818576	2.58	41.11±0.34	43.69	38.66	nan	3.64±0.35	False	1.30
9881-1901	204.806913	24.893076	0.0282062	2.53	39.79±0.32	41.81	nan	nan	0.61±0.37	True	0.00
9883-12701	255.523309	31.797429	0.0650401	2.41	40.94±0.26	42.83	38.24	0.85±0.81	2.37±0.79	True	0.86
9888-12701	235.475823	28.133979	0.0332197	2.56	40.70±0.28	42.61	38.16	0.52±0.39	2.98±0.52	True	0.60
9893-6102	256.196769	24.583993	0.0425203	2.52	39.06±74.36	42.54	nan	nan	nan	True	0.00
8656-12705	7.387001	-1.095700	0.0585413	2.45	40.72±0.46	43.45	38.77	nan	3.87±0.60	True	1.77
8656-12702	7.085553	-0.217869	0.0612581	2.49	40.28±0.38	42.98	nan	nan	3.40±0.40	False	0.00
9498-3703	120.016894	23.437849	0.0291978	2.71	40.95±0.25	42.68	38.22	nan	1.07±0.45	True	2.12
10216-3704	117.239526	17.577121	0.0286623	2.75	40.25±0.26	42.37	38.15	0.34±0.42	1.01±0.39	True	1.61
10216-12704	118.162300	18.321606	0.0449364	2.65	41.39±0.29	42.85	38.81	0.41±0.56	12.25±4.03	True	2.51
10218-1902	119.207582	17.380303	0.0364051	2.34	40.57±0.28	42.67	nan	nan	3.36±0.86	False	0.00
10221-6104	124.698298	24.537430	0.024877	2.59	39.73±0.28	42.11	nan	nan	1.09±0.49	True	0.00
9503-12701	119.972832	23.390083	0.029143	2.47	41.06±0.34	43.77	38.68	nan	3.38±0.38	False	2.17
9503-6102	120.996684	23.755667	0.0293812	2.47	41.22±0.27	42.66	37.75	nan	3.34±0.27	False	0.68
9503-3704	121.037072	24.558611	0.0438319	2.41	40.19±0.37	42.48	nan	nan	3.27±0.06	False	0.00
9499-12703	118.423230	26.492699	0.0374233	2.92	40.24±0.32	42.84	nan	nan	3.31±0.24	False	0.00
9499-6104	120.082382	26.701442	0.0278268	2.91	40.97±0.30	43.07	37.86	0.99±0.33	2.11±0.34	True	0.66
9499-6101	118.071091	25.669081	0.0453547	2.96	40.58±0.31	42.52	nan	nan	3.44±0.40	False	0.00
10215-1902	123.857378	37.340519	0.0397304	2.25	40.18±0.30	42.27	nan	nan	1.10±0.61	True	0.00
9495-1901	122.938744	23.473828	0.015734	2.47	39.57±0.27	41.20	nan	nan	2.90±0.09	False	0.00
8723-6104	130.407776	54.918571	0.044562	2.29	40.65±41.29	43.48	nan	nan	nan	False	0.00
9489-6104	126.084373	20.533242	0.0199314	2.42	40.41±0.35	42.31	nan	nan	3.08±0.07	False	0.00
8998-12705	163.663838	47.862282	0.0728894	2.65	41.08±0.31	43.47	nan	nan	3.63±0.20	False	0.00
8981-6104	187.419144	36.199417	0.0717308	2.54	41.10±0.34	42.90	nan	nan	3.60±0.38	False	0.00

Table 1 – *continued*

plateifu	ra degree	dec degree	z	g_{PSF}(FWHM) arcsec	$\log L_{[O\,III]}$ erg/s	$\log L_{8\mu m}$ erg/s	$\log L_{1.4GHz}$ erg/s	R_{15} (kpc)	R_{16} (kpc)	resolved	radio loudness
8988-6102	186.251194	40.157312	0.0735606	2.51	40.99±0.39	43.38	39.24	nan	3.65±0.80	False	4.35
10514-12705	144.628220	2.573280	0.0234383	2.52	40.24±0.36	42.54	nan	0.17±0.26	1.20±0.26	True	0.00
10514-9102	145.151611	3.577021	0.0164514	2.44	41.14±0.27	42.89	37.63	nan	3.10±0.09	False	0.40
10510-12704	179.117267	55.125209	0.00371352	2.53	39.76±0.24	41.85	36.22	0.17±0.04	0.42±0.09	True	0.10
10510-6103	177.778667	55.078717	0.0194702	2.57	40.82±0.29	42.91	38.02	nan	3.23±0.28	False	0.59
10493-3704	126.015364	51.904331	0.0314512	2.52	41.06±0.24	42.59	37.33	0.62±0.35	1.65±0.36	True	0.73
9884-3704	206.669999	52.476814	0.0291777	2.47	41.17±0.24	42.51	37.51	1.03±0.31	2.24±0.34	True	0.37
10494-12701	126.358456	53.968934	0.0641308	2.18	41.17±0.28	42.99	nan	nan	3.84±1.51	False	0.00
10508-12703	184.652029	51.414732	0.0471993	2.72	41.29±0.28	43.21	nan	1.09±0.53	2.30±0.69	True	0.00
10508-6101	183.371990	50.741529	0.0307574	2.76	40.59±0.25	42.87	39.48	0.19±0.43	2.30±0.90	True	12.15
10492-12702	124.064090	57.530542	0.0271824	2.75	40.21±0.35	42.47	nan	nan	0.04±0.06	True	0.00
10492-6103	122.972981	57.951893	0.0277501	2.75	41.66±0.24	43.33	38.48	1.69±0.30	3.04±1.47	True	5.81
9882-9102	207.608226	23.456934	0.0557381	2.59	40.95±0.27	42.58	nan	nan	2.73±1.14	True	0.00
9882-3701	206.626565	23.097190	0.0299905	2.61	39.95±0.34	42.44	37.44	nan	0.53±0.59	True	0.25
10503-12703	160.228870	5.991890	0.0276125	2.47	40.79±0.47	43.02	38.53	0.76±0.37	6.74±1.50	True	3.12
9091-3704	241.944669	25.537511	0.0406597	2.36	41.39±0.28	42.92	38.08	1.90±0.72	3.31±2.05	True	3.42
9091-12703	240.044496	27.605140	0.03303	2.42	40.64±0.42	42.47	nan	nan	3.27±0.16	False	0.00
8337-1901	214.096447	38.190986	0.134659	2.35	41.70±0.34	43.82	39.23	0.51±12.60	3.79±2.71	True	4.63
9885-3703	241.152724	23.663184	0.031032	2.34	40.48±0.27	42.61	nan	nan	3.23±0.09	False	0.00
8334-3703	213.230230	39.312652	0.0250682	2.50	39.67±0.60	42.12	nan	nan	1.60±1.63	True	0.00
8260-1901	182.253728	42.475257	0.02364	2.35	40.08±0.42	41.30	nan	nan	3.08±0.10	False	0.00
9892-3703	248.383907	24.984722	0.0594202	2.46	41.34±0.28	43.04	nan	1.05±0.66	2.59±0.77	True	0.00
8324-6104	198.958904	46.338830	0.0573434	2.39	41.14±0.28	43.38	38.82	0.50±0.87	11.87±12.49	True	4.11
8614-12703	258.118529	35.884086	0.026418	2.63	41.00±0.30	42.88	nan	nan	3.31±0.24	False	0.00
8614-3703	257.001371	36.344421	0.0362362	2.62	40.65±0.26	42.77	38.48	0.37±0.47	1.80±0.41	True	2.40
9092-1902	240.779508	24.523990	0.0466923	2.33	41.16±0.28	43.16	38.12	nan	3.56±0.62	False	1.75
9032-12701	240.475078	31.892062	0.0449613	2.47	41.47±0.32	43.11	nan	1.13±1.34	3.78±2.34	True	0.00
9032-12702	241.452770	30.717059	0.0553885	2.42	41.16±0.28	42.63	nan	nan	2.43±0.69	True	0.00
8593-12705	226.937461	51.452832	0.0459164	2.75	41.77±0.45	43.34	38.31	2.80±0.57	12.74±2.02	True	0.74
9090-9102	243.073394	28.429551	0.0531379	2.62	40.39±0.40	42.82	39.87	nan	3.44±0.46	False	25.73
9090-3701	241.717361	27.927542	0.0460252	2.60	41.39±0.27	43.57	38.29	nan	3.54±0.43	False	1.49
8651-1902	313.902141	-0.636586	0.0535281	2.48	41.45±0.25	43.11	39.14	nan	3.35±0.52	False	6.71